



PAPER

[View Article Online](#)
[View Journal](#) | [View Issue](#)Cite this: *Dalton Trans.*, 2024, **53**, 5212

Fabrication of a ZIF-on-lamella-zeolite architecture as a highly efficient catalyst for aldol condensation†

Tianlong Wang,^a Lin-an Liu,^a Huifang Wu,^a Jiaxing Zhang,^b Ziyi Feng,^a Xin Yan,^a Xinyu Wang,^a Guoying Han,^a Xiao Feng,^a Limin Ren ^{*a} and Xinwen Guo ^{*b}

Designing composite catalysts that harness the strengths of individual components while mitigating their limitations is a fascinating yet challenging task in catalyst engineering. In this study, we aimed to enhance the catalytic performance by anchoring ZIF-67 nanoparticles of precise sizes onto lamella Si-MWW zeolite surfaces through a stepwise regrowth process. Co ions were initially grafted onto the zeolite surface using ultrasonication, followed by a seed-assisted secondary growth method. Si-MWW proved to be the ideal zeolite support due to its thin layered structure, large external surface area and substantial lateral dimensions. The abundant Si–OH groups on its surface played a crucial role in securely binding Co ions, limiting size growth and preventing undesirable ZIF-67 aggregation. The resulting ZIF-67/MWW composite with finely dispersed nano-scale ZIF-67 particles exhibited a remarkable catalytic performance and stability in the aldol condensation reactions involving acetone and various aldehydes. This approach holds promise for designing MOF/zeolite composite catalysts.

Received 31st January 2024,
Accepted 7th February 2024

DOI: 10.1039/d4dt00288a

rsc.li/dalton

1. Introduction

Metal–organic frameworks (MOFs), renowned for their adjustable compositions and pore architectures, have ushered in an intriguing platform for crafting functional materials.^{1–5} Among these, zeolitic imidazole frameworks (ZIFs), a subset of MOFs, stand out.^{6–10} Comprising transition metals (such as Co, Cu and Zn) interconnected by N-rich imidazole ligands, ZIFs exhibit exceptional chemical and thermal stability, rendering them highly suitable for deployment under demanding conditions. Scaling down ZIFs to the nano level provides significant benefits. This includes enhancing the accessibility of active sites, shortening diffusion pathways and curbing unintended side reactions.^{11–13} However, the catalytic efficacy and durability of nano-sized catalysts often suffer due to the tendency of small nanoparticles to aggregate, either during preparation or catalytic processes.^{14,15} To surmount this limitation, an effective solution is to immobilize these nano-sized catalysts onto supports, creating supported catalysts.^{14,16–19}

Zeolites,^{20–22} in virtue of their high surface areas, exceptional thermal and hydrothermal stabilities, as well as adjustable acidity, have emerged as compelling hosts for supporting active MOFs in the creation of composite catalysts.^{17,18,23} To illustrate, Co-MOF nanosheets were meticulously affixed onto the external facets of the ZSM-5 zeolite, yielding a composite catalyst that demonstrated an enhanced olefin epoxidation activity.²⁴ Furthermore, the Wattanakit group made efforts to construct zeolite/MOF hybrid materials, such as FAU/ZIF-8¹⁷ and Fe-ZSM-5@ZIF-8,¹⁸ hinging on amine-functionalized zeolites. These composite structures ingeniously amalgamated the functionalities of both constituents, zeolite and MOF, resulting in exceedingly auspicious catalytic performances.

It's important to note that a hierarchical zeolite structure is preferred as a support over a pure microporous one, primarily due to its capacity to mitigate mass transfer resistance and provide a larger outer surface, enhancing the dispersion and carrying the abilities of nanoparticles.^{17,25,26} However, the utilization of hierarchical zeolites often involves intricate synthesis procedures or increased costs. In this context, lamellar zeolites emerge as an excellent alternative for immobilizing nano-sized entities, sidestepping the complexities associated with hierarchical zeolite preparation. Among these, the MWW zeolite,^{27–32} the most widely employed lamellar zeolite, offers an ideal support. Comprising 10-membered ring (10-MR) channels and 12-MR pockets and cups, its flat, expansive and thin structure, coupled with the abundance of surface Si–OH

^aState Key Laboratory of Fine Chemicals, School of Chemistry, Dalian University of Technology, Dalian 116024, PR China. E-mail: lren@dlut.edu.cn^bState Key Laboratory of Fine Chemicals, Frontiers Science Center for Smart Materials, School of Chemical Engineering, Dalian University of Technology, Dalian, 116024, PR China. E-mail: guoxw@dlut.edu.cn†Electronic supplementary information (ESI) available. See DOI: <https://doi.org/10.1039/d4dt00288a>

groups, makes it exceptionally well-suited to immobilize nano-sized active species.^{33,34} The substantial presence of surface Si-OH groups in the MWW zeolite obviates the need for a functionalization step. This not only prevents pore blockage, but also eliminates the increased costs associated with the use of functionalizing reagents.

Building upon our prior expertise in ZIF synthesis and MWW zeolite preparation,^{35,36} we developed a step-wise seed-assisted regrowth methodology to engineer a ZIF-67/MWW composite, involving the “hatching” of ZIF-67 seeds onto the surface of the Si-MWW zeolite through ultrasonication, followed by a secondary growth process. As a result, finely controlled ZIF-67 nanoparticles became uniformly and durably affixed to the layered structure of the Si-MWW zeolite through precise modulation. Simultaneously, these Si-OH groups effectively restricted particle dimensions and thwarted undesirable aggregation. The resulting ZIF-67/MWW composite, featuring both acid and base functionalities, exhibits remarkable catalytic performance and notable recyclability in the aldol condensation reaction between various aldehydes and acetone, for making value-added downstream products.

2. Experimental

2.1 Synthesis of materials

2.1.1 Synthesis of Si-MWW. The Si-MWW zeolite was synthesized following previously reported procedures.³⁶ Initially, 12.88 g of *N,N,N*-trimethyl-1-adamantammonium hydroxide (TMAdaOH, 25 wt%) was mixed with 48.31 g of deionized water. Then, 1.87 g of hexamethyleneimine (HMI, 98 wt%) was added to the above solution under stirring. Subsequently, 3.66 g of fumed silica (Cab-o-sil M5) was added to the mixture and stirred for 12 h. The resulting mixture was transferred to a 50 mL PTFE lined stainless steel autoclave and heated at 150 °C for 5 d while rotating at 30 rpm. After hydrothermal crystallization, the sample was filtered, washed with deionized water until the pH was less than 8, and dried at 80 °C. Finally, the dried sample was calcined at 600 °C in a muffle furnace for 10 h to obtain Si-MWW.

2.1.2 Synthesis of ZIF-67. For the typical preparation of ZIF-67, Co(NO₃)₂·6H₂O (1.88 g, 6.33 mmol) and 2-methylimidazole (Hmim) (0.43 g, 5.82 mmol) were separately dissolved in 50 mL of ethanol. The solutions were mixed and vigorously stirred for 6 h at room temperature. The resulting product was separated by centrifugation at 8000 rpm, washed with ethanol, and dried at 80 °C.

2.1.3 Synthesis of the ZIF-67/MWW(U) composite. 0.1 g of Si-MWW was dispersed in 10 mL of ethanol and stirred under ultrasonication at room temperature for 20 min, forming suspension A. Solution B was prepared by dissolving 0.35 g of Co(NO₃)₂·6H₂O in 10 mL of ethanol. Suspension A and solution B were mixed and subjected to ultrasonication for 60 min, followed by centrifugation at 6000 rpm for 5 min to separate the solid product. Next, a solution of 2-methylimidazole (1 g per 40 mL of ethanol) was added to the solid product, and the

mixture was treated by ultrasonication at room temperature for 60 min. Finally, the solid product was collected by centrifugation, washed with ethanol three times, and dried at 80 °C for 12 h. The obtained sample was denoted as ZIF-67/MWW(U), where U represents the ultrasonication process.

2.1.4 Synthesis of the ZIF-67/MWW(R) composite. The above centrifugation product (0.106 g) of ZIF-67/MWW(U) was dispersed in a solution containing 1 g of 2-methylimidazole in 10 mL of ethanol, and the resulting mixture was sonicated at room temperature for 10 min, marked as Suspension A. Solution B was prepared by dissolving 0.35 g of Co(NO₃)₂·6H₂O in 20 mL of ethanol. Suspension A and solution B were mixed and vigorously stirred for 120 min, followed by centrifugation at 6000 rpm for 5 min to separate the solid product. Finally, the product was washed with ethanol three times and dried at 80 °C for 12 h. The obtained product was denoted as ZIF-67/MWW(R), where R represents the regrowth process.

2.1.5 Synthesis of the ZIF-67/MWW(T) composite. The above centrifugation product (0.154 g) of ZIF-67/MWW(R) was dispersed in a solution containing 1 g of 2-methylimidazole in 10 mL of ethanol, and the resulting mixture was sonicated at room temperature for 10 min, marked as Suspension A. Solution B was prepared by dissolving 0.35 g of Co(NO₃)₂·6H₂O in 20 mL of ethanol. Suspension A and solution B were mixed and vigorously stirred for 120 min, followed by centrifugation at 6000 rpm for 5 min to separate the solid product. Finally, the product was washed with deionized water and ethanol three times, respectively, and dried at 80 °C for 12 h. The obtained product was denoted as ZIF-67/MWW(T), where T represents that the regrowth process was performed twice.

2.2 Catalysis test

In a typical run, 0.1 g (0.8 mmol) of 5-HMF, 5 mL of acetone, 0.05 g of *N*-dodecane and a certain amount of catalyst were added to a temperature-controlled 50 mL autoclave and sealed. The reactor was heated to 150 °C for the desired time. Moreover, furfural, benzaldehyde, cinnamaldehyde, and some electron-donating or -withdrawing group substituted aromatic aldehydes as substrates were also explored. Then, the product was separated by filtering the catalyst from the mixture and subsequently analyzed by gas chromatography (GC Agilent, 8860) equipped with an HP-5 MS capillary column (0.32 mm × 0.25 μm × 30 m) and an FID detector.

2.3 Characterization

Powder X-ray diffraction (PXRD) patterns were collected using a Rigaku SmartLab 9 kW diffractometer (45 kV, 200 mA) with Cu Kα radiation ($\lambda = 1.5406 \text{ \AA}$). Data were collected in the 2θ range from 5° to 40° with a scan speed of 8° min⁻¹ and a step size of 0.02°. N₂ adsorption-desorption isotherms were measured using a Micromeritics 3Flex instrument at -196 °C. All samples were degassed at 200 °C under vacuum for 5 h prior to measurement. The total surface area was evaluated based on the BET equation. TEM was conducted using a



JEM-F200 field emission transmission electron microscope at 200 kV. SEM was conducted using a 7610 Plus field emission scanning electron microscope at 10 kV. ICP-OES was performed using a PerkinElmer/NexION 500 and the samples were dissolved in hydrofluoric acid and diluted to 25 mL with water. UV-vis spectra were recorded on a Shimadzu UV 2600 using barium sulfate as the reference. *In situ* diffuse reflectance infrared Fourier transform (DRIFT) spectroscopy was performed using a Fourier transform infrared (FTIR) spectrometer (Thermo Scientific, Nicolet iS50) equipped with a high-temperature reaction chamber and a mercury cadmium telluride (MCT) detector with a resolution of 8 cm^{-1} and an accumulation of 32 scans. The catalysts were exposed to Ar gas with a flow rate of 30 mL min^{-1} . Then, the background spectrum was obtained at room temperature and the spectra were recorded. Fourier transform infrared (FTIR) spectra were collected in KBr media between 4000 and 400 cm^{-1} on a ThermoFisher 6700. The sample was first mixed with KBr at a mass ratio of $1:100$ and was ground uniformly. After that, the mixture was pressed into a tablet for characterization. Temperature programmed desorption of ammonia (NH_3 -TPD) was performed on a PCA-1200 chemical adsorption instrument. 0.065 g of catalyst was placed at the bottom of the tube and degassed at $100\text{ }^\circ\text{C}$ for 120 min , then cooled to $40\text{ }^\circ\text{C}$ for NH_3 adsorption. After removing the physisorbed NH_3 , the NH_3 -TPD data were recorded from $40\text{ }^\circ\text{C}$ to $300\text{ }^\circ\text{C}$ with a ramp of $10\text{ }^\circ\text{C min}^{-1}$.

3. Results and discussion

3.1 Synthesis and characterization of the ZIF-67/MWW composite

Scheme 1 illustrates the synthesis process of the ZIF-67/MWW composite. First, Co^{2+} ions, which serve as the metal source of ZIF-67, were mixed with Si-MWW under sonication to modify

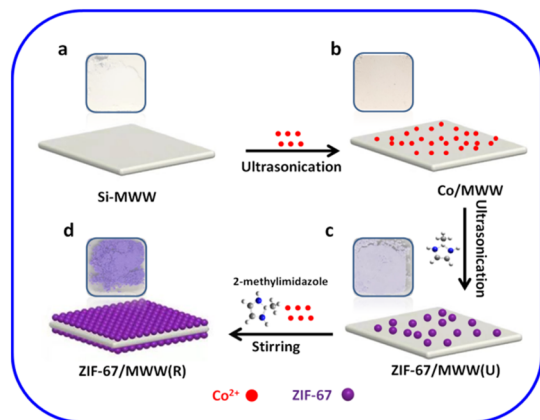
the surface of Si-MWW. Then, the linker 2-methylimidazole was added to coordinate with the Co^{2+} ions on the surface of the Si-MWW zeolite, resulting in the formation of ZIF-67/MWW(U). Due to the limited Co^{2+} content on the Co/MWW surface, the initial growth of ZIF-67 through sonication was minimal (Table 1). To achieve substantial growth of ZIF-67, a secondary growth process was conducted using ZIF-67/MWW(U) as seeds in the ZIF-67 growth solution. As depicted in Scheme 1, the solid samples gradually changed color from white to reddish, lavender and purple. The reddish color is associated with the Co^{2+} ions, indicating Co^{2+} grafted on Si-MWW. After the addition of linkers, ZIF-67 is formed, which is typically purple in color (Fig. S1, ESI†). The deepening of the color from lavender to purple suggests an increased ZIF-67 content in the ZIF-67/MWW mixture (Table 1).

The formation of the ZIF-67/MWW structure is further confirmed by characterization at multiple scales. Fig. 1a shows the XRD patterns of samples at different stages. Throughout the process, the characteristic peaks of Si-MWW are well preserved. Notably, the main peak of Si-MWW and ZIF-67 overlaps at $2\theta = 7.4^\circ$.^{37,38} Only a weak diffraction peak corresponding to the (002) peak of ZIF-67 is detectable at $2\theta = 12.8^\circ$ in ZIF-67/MWW(U) obtained after the ultrasonication stage. Prominent characteristic ZIF-67 diffraction peaks ($2\theta = 12.8^\circ$ and 18.0°) are observed in ZIF-67/MWW(R) obtained after the secondary growth. Consistent with the photos, initial growth of ZIF-67 occurs after the sonication treatment, and the regrowth process leads to a substantial increase in ZIF-67 content (Table 1). N_2 physisorption was used to study the textural properties of the products after different treatment procedures. As shown in Fig. 1b, both Si-MWW and pure ZIF-67 display

Table 1 Weight and Co content of the solids collected at different growth stages for preparing ZIF-67/MWW

Sample	Initial weight (g)	Product weight (g)	Co content ^a (wt%)
ZIF-67/MWW(U)	0.100	0.106	1.82
ZIF-67/MWW(R)	0.106	0.154	13.4
ZIF-67/MWW(T)	0.154	0.288	28.0

^a The Co content was determined by ICP analysis.



Scheme 1 Schematic illustration of the synthesis of the ZIF-67/MWW composite, with photographs showing the color change at different synthesis stages. (a) Si-MWW, (b) Co grafted on Si-MWW (Co/MWW), (c) after ultrasound growth of ZIF-67 (ZIF-67/MWW(U)), and (d) the sample after regrowth (ZIF-67/MWW(R)).

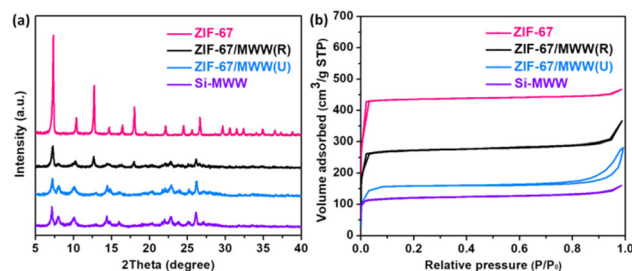


Fig. 1 (a) Powder X-ray diffraction patterns and (b) N_2 adsorption-desorption isotherms of Si-MWW, ZIF-67/MWW(U), ZIF-67/MWW(R) and ZIF-67.



typical type-I adsorption-desorption isotherms due to their microporous structures, with ZIF-67 exhibiting a higher adsorbed volume. The isotherms of ZIF-67/MWW(U) and ZIF-67/MWW(R) lie between those of Si-MWW and ZIF-67. Clearly, ZIF-67/MWW(R) exhibits higher N_2 uptake than ZIF-67/MWW(U) (Table 2), attributed to its higher ZIF-67 content (Table 1), consistent with the XRD result.

SEM imaging and TEM imaging were conducted to examine the morphology of the resulting materials. As shown in Fig. 2a, the Si-MWW zeolite exhibits a thin sheet-like morphology with a smooth surface and large in-plane dimensions, approximately 2–5 μm . After the initial ultrasonication treatment with Co^{2+} and the linker, extremely small particles (<20 nm) with a limited content were deposited on the surface of Si-MWW (Fig. 2b). Based on the XRD and N_2 physisorption results, these tiny particles are identified as ZIF-67 crystals. Upon further regrowth of ZIF-67/MWW(U), a more extensive coverage of the Si-MWW surface is observed in the SEM image (Fig. 2c) and TEM image (Fig. 2d) of ZIF-67/MWW(R). Notably, the

Table 2 Structural properties of the Si-MWW, ZIF-67 and ZIF-67/MWW samples

Sample	S_{BET} ($\text{m}^2 \text{g}^{-1}$)	S_{ext}^a ($\text{m}^2 \text{g}^{-1}$)	V_{micro}^a ($\text{cm}^3 \text{g}^{-1}$)	V_{meso}^b ($\text{cm}^3 \text{g}^{-1}$)	V_{total}^c ($\text{cm}^3 \text{g}^{-1}$)
Si-MWW	460	57	0.16	0.09	0.25
ZIF-67/MWW(U)	500	46	0.22	0.17	0.39
ZIF-67/MWW(R)	978	80	0.35	0.19	0.54
ZIF-67	1674	46	0.65	0.07	0.72

^a External surface areas (S_{ext}) and micropore volumes (V_{micro}) were determined using t -plot analysis. ^b Mesopore volumes (V_{meso}) were calculated as $V_{\text{total}} - V_{\text{micro}}$. ^c Total pore volumes were determined at $P/P_0 = 0.99$.

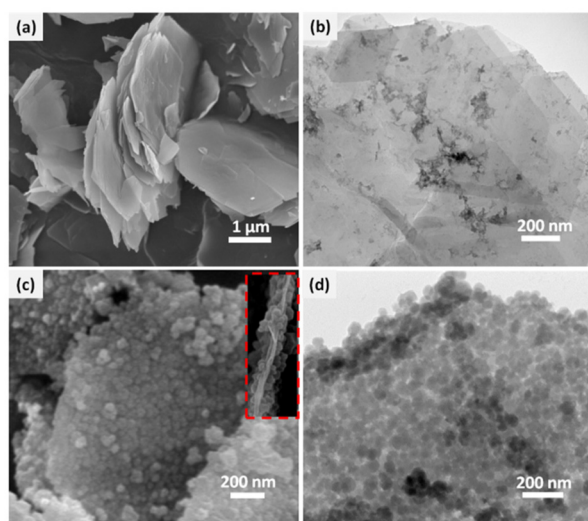


Fig. 2 SEM images of (a) Si-MWW and (c) ZIF-67/MWW(R) and the inset of (c) ZIF-67/MWW(R) after sonication; TEM images of (b) ZIF-67/MWW(U) and (d) ZIF-67/MWW(R).

initial ZIF-67 nanoparticles of ZIF-67/MWW(U) increase in both size and quantity during the regrowth treatment. The ZIF-67 nanoparticles, with an average size of approximately 80 nm, are tightly packed on the surface of the Si-MWW zeolite, and no particle peeling-off is observed even after intense sonication (Fig. 2c inset). The TEM image (Fig. 2d) clearly shows that the ZIF-67 nanoparticles are uniformly dispersed on the Si-MWW sheet surface, without agglomeration or multilayer stacking. The EDS mapping images of the ZIF-67/MWW(R) sample obtained in SEM mode (Fig. 3) reveal a homogeneous distribution of Si, O, Co, C and N elements in the ZIF-67/MWW(R) composite. Specifically, the distribution of Co, C and N elements matches well with the Si-MWW region, indicating that the ZIF-67 nanoparticles are preferentially attached to the Si-MWW surface. It is worth mentioning that, in addition to the location fixation, the supported growth strategy also results in a size-confining effect. Compared to ZIF-67 prepared using the conventional growth method (size around 300 nm, Fig. S2, ESI[†]), the ZIF-67 particle size (80 nm) on ZIF-67/MWW(R) is significantly reduced.³⁹ This reduction can be attributed to the beneficial effect of surface Si-OH groups on grafting Co ions, which coordinate with the linkers to generate tiny ZIF-67 crystals on the Si-MWW surface during the sonicated growth stage. In the secondary growth stage, these tiny ZIF-67 particles act as seeds for guiding the further growth of ZIF-67 crystals. Notably, the secondary growth step can be rapidly completed in only 0.5 h at room temperature (Fig. 2d), which can be explained by the promoting effect of the seeds, requiring a much lower energy barrier compared to the regular spontaneous growth of ZIF-67.

The FTIR spectra of ZIF-67, ZIF-67/MWW(U), ZIF-67/MWW(R) and Si-MWW are shown in Fig. 4a. The characteristic structural vibration peaks of the Si-MWW framework (D6R: 610 and 560 cm^{-1} , T-O bending vibration in TO_4 : 450 cm^{-1}) are well preserved after each growth stage.⁴⁰ Additionally, the characteristic peaks (1305, 1417 and 1455 cm^{-1}) corresponding to the stretching and bending modes of 2-methylimidazole are observed in ZIF-67/MWW(R), but they are too weak to be detected in ZIF-67/MWW(U).^{41,42} Similarly, the Co-N stretching peak at 424 cm^{-1} , resulting from the interaction of cobalt ions and 2-methylimidazole linkers, is observed in ZIF-67/

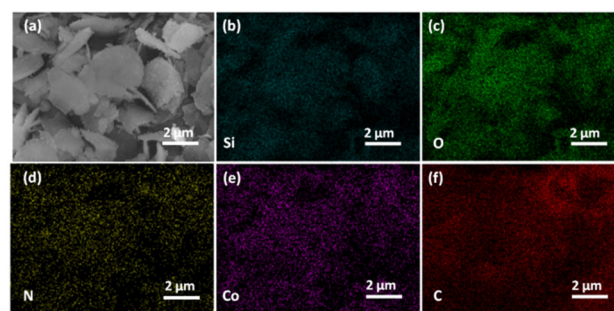


Fig. 3 (a) SEM and (b–f) EDS elemental mapping images of ZIF-67/MWW(R).



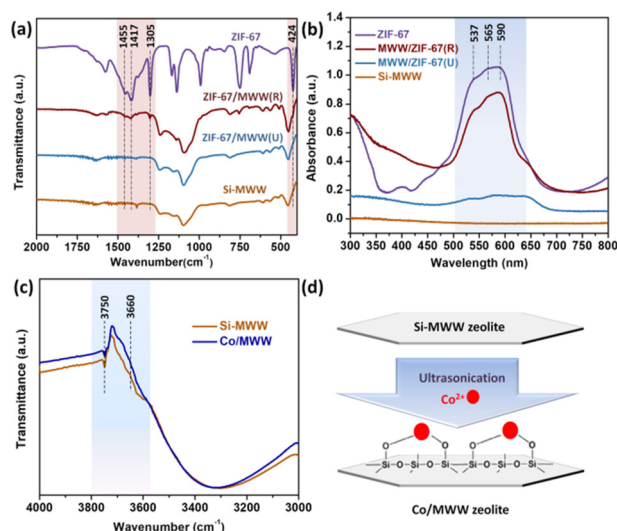


Fig. 4 (a) FTIR and (b) UV-vis spectra of Si-MWW, ZIF-67, ZIF-67/MWW (U) and ZIF-67/MWW(R); (c) *in situ* FTIR spectra of the hydroxyl region of Si-MWW and Co/MWW and (d) schematic diagram depicting the process of converting Si-MWW to Co/MWW.

MWW(R) but not detectable in ZIF-67/MWW(U) due to the limited ZIF-67 content.⁴³ UV-vis spectroscopy was performed to investigate the coordination status of the 2-methylimidazole ligand and cobalt ions in ZIF-67/MWW composites. As shown in Fig. 4b, three main absorption peaks (537, 565 and 590 nm) are observed in pure ZIF-67, which are attributed to the $^4A_2(F) \rightarrow ^4T_1(P)$ transition of Co²⁺ ions in tetrahedral coordination environments, known as the spin coupling triple peaks.³⁹ Similar absorption peaks are present in ZIF-67/MWW(R), indicating the presence of ZIF-67 in the ZIF-67/MWW(R) composite. Due to the low content of ZIF-67 on the surface of Si-

MWW, the relevant adsorption peaks are very weak in ZIF-67/MWW(U), consistent with the TEM and XRD results.

Collectively, the above characterization results confirmed the formation of the ZIF-67/MWW composite, with ZIF-67 particles uniformly anchored on the surface of the Si-MWW sheet. It is reasonable to believe that the initial step of Co grafting is crucial. To investigate the interaction between Si-MWW and Co ions, Si-MWW and Co/MWW samples were analyzed using IR spectroscopy after *in situ* heating at 500 °C (Fig. 4c). Both samples exhibit a sharp band at 3750 cm⁻¹, attributed to external silanol groups.^{44,45} Additionally, a broad peak at 3660 cm⁻¹, related to weakly hydrogen-bonded terminal silanols, is also observed.^{46,47} After the ultrasonication treatment with Co ions, the peak intensities at 3660 and 3750 cm⁻¹ decrease, indicating that the cobalt ions interact with the silicon hydroxyl groups on the Si-MWW zeolite surface (Fig. 4d).³⁶

Apart from the Si-OH rich feature of Si-MWW, the flat surface and large in-plane dimension also contribute to its optimal support capability, providing ample space for holding the nanoparticles. To confirm the central role of Si-MWW in constructing the special hybrid structure, pure silica zeolites with different structures and surface properties (Si-Beta,⁴⁸ Silicalite-1⁴⁹ and Si-SPP⁵⁰) were used to prepare the composite using the same synthesis strategy. The XRD patterns (Fig. S3, ESI†) confirm the presence of both ZIF-67 and zeolite structures in the products. Si-Beta zeolite, a three-dimensional hydrophobic zeolite prepared under fluorine-mediated conditions, was chosen as a representative. It has rare Si-OH on its surface. When Si-Beta (Fig. 5a) was used instead of Si-MWW and subjected to similar treatment procedures, aggregated ZIF-67 nanoparticles were randomly attached to part of the Si-Beta surface and scattered around (Fig. 5d), indicating a poor supporting effect. Given that Si-

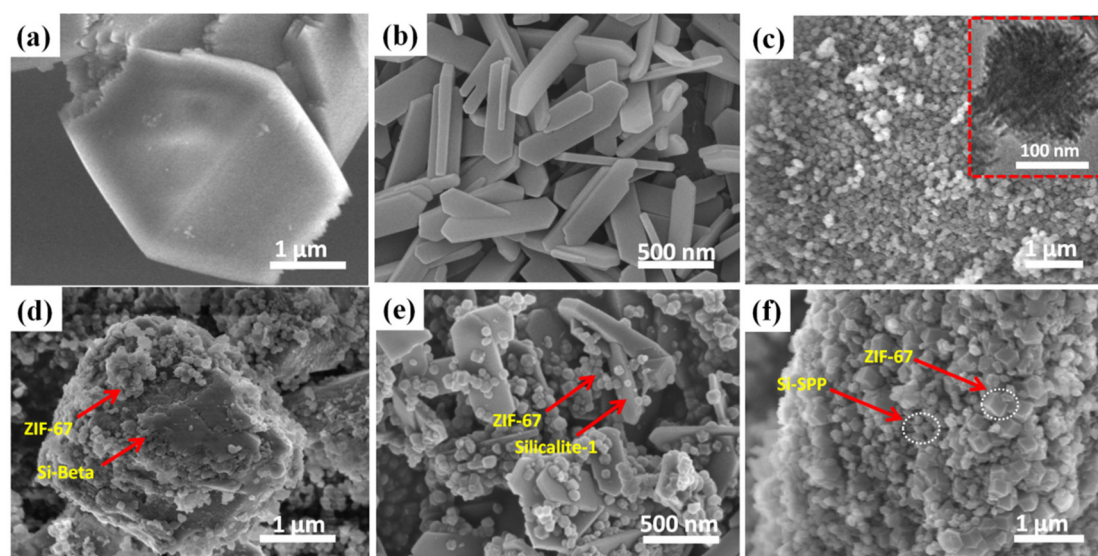


Fig. 5 SEM images of (a) Si-Beta, (b) Silicalite-1, (c) Si-SPP (inset shows the corresponding TEM image), (d) ZIF-67/Beta, (e) ZIF-67/Silicalite-1 and (f) ZIF-67/SPP.



Beta lacks the large platy surface, Silicalite-1 zeolite with a sheet-like morphology (Fig. 5b) and a similar hydrophobic surface was attempted as the support. Despite the large lateral surface of Silicalite-1, ZIF-67 nanoparticles mainly existed in an aggregated form, disorderly distributed and mixed with Silicalite-1 zeolite (Fig. 5e), leaving a large portion of the Silicalite-1 surface uncovered. Apparently, when the same growth procedures were performed over the F-mediated zeolites, it was hard to achieve the same attached growth pattern as happened for ZIF-67 on Si-MWW, which is mainly attributable to the insufficient surface silica hydroxyl groups on their surface, thus failing to interact with Co ions to realize the anchoring of ZIF-67 nanoparticles.

FTIR spectra (Fig. S4, ESI†) confirmed the rarity of silica hydroxyl species of both Si-Beta and Silicalite-1, in significant contrast to Si-MWW and Si-SPP, where two key vibration bands around 3660 cm^{-1} and 3470 cm^{-1} were displayed, attributed to the external silanol groups and internal silanol groups within the framework,^{51–53} respectively. In this regard, the self-pillared pentasil (SPP) zeolite, with a spherical size of about 100 nm, composed of orthogonal inter-grown ultra-thin nanosheets with abundant surface silica hydroxyl groups was tested as a support (Fig. 5c). The obtained product is composed of closely mixed ZIF-67 and Si-SPP particles (Fig. 5f). Due to the limited size of Si-SPP zeolite, it was hard for ZIF-67 particles to be attached on. Overall, it is evident that the lamellar MWW zeolite, with a high diameter-to-thickness ratio and rich Si-OH groups, is the optimal choice as the carrier.

As mentioned earlier, a secondary growth stage after ultrasound treatment significantly enhanced the coverage level (from scattering to tight packing) and increased the size (from 20 nm to 80 nm) of ZIF-67 nanoparticles on the Si-MWW surface (Fig. 2c), attributed to the provision of more nutrients. This indicates that the size and packing level of ZIF-67 nanoparticles can be controlled by adjusting the supply of nutrients. This manipulation can be achieved by tuning the regrowth cycles or adjusting the concentration of precursors during the regrowth procedure. As expected, two rounds of secondary growth of ZIF-67/MWW(U) resulted in a more densely packed ZIF-67 layer with a thickness above 200 nm (Fig. 6a inset) on the surface of the Si-MWW zeolite (Fig. 6a). By fixing the regrowth time as one and reducing the concentration of precursors to 1/2, 1/4 and 1/8 of the original level, respectively, the dispersion and particle size of ZIF-67 changed accordingly (Fig. 6b–d). Specifically, the average sizes of ZIF-67 nanoparticles on the surface of Si-MWW decreased from 80 nm in ZIF-67/MWW(R) to 57 nm in ZIF-67/MWW(1/2), 35 nm in ZIF-67/MWW(1/4) and 27 nm in ZIF-67/MWW(1/8). Alongside, the density of the particles also decreased. Unlike the nearly fully covered surface of Si-MWW in ZIF-67/MWW(R), there was still space between ZIF-67 nanoparticles in ZIF-67/MWW(1/2, 1/4 and 1/8). XRD patterns of different ZIF-67/MWW samples agreed with the SEM results, showing that samples with more attached ZIF-67 exhibited a stronger ZIF-67 peak strength (Fig. S5, ESI†).

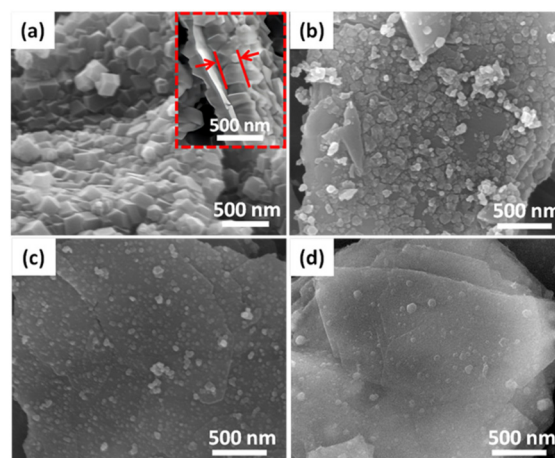


Fig. 6 SEM images of ZIF-67/MWW of (a) ZIF-67/MWW(T) obtained by conducting two times of regrowth (inset: side view of ZIF-67/MWW(T)); and ZIF-67/MWW products obtained with different concentrations of Hmim and Co ions: (b) ZIF-67/MWW(1/2), (c) ZIF-67/MWW(1/4) and (d) ZIF-67/MWW(1/8).

3.2 Catalytic study

5-Hydroxymethyl furfural (HMF) is a key platform chemical synthesized from hexoses, and can be converted into a high value-added compound, 4-[5-(hydroxymethyl)-2-furanyl]-3-buten-2-one (HMB), *via* an aldol condensation process.^{54–57} HMB can be further hydrogenated to produce a range of linear alkanes, which could act as efficient jet fuel additives. Herein, ZIF-67/MWW composites were used as catalysts for the aldol condensation reaction, involving the reaction of HMF with acetone to produce HMB as the main product.

As shown in Table 3, only a 3.3% conversion was achieved in the absence of any catalyst (Table 3, entry 1). When the

Table 3 A comparison of different catalysts for the aldol condensation reaction

Entry	Catalyst	Conversion (%)	Yield ^a (%)	Selectivity (%)
1	Blank	3.3	0	0
2	Si-MWW	15.7	4.5	28.6
3	Co/MWW	30.7	8.4	27.4
4	ZIF-67/MWW(U)	64.9	56.5	87.0
5	ZIF-67/MWW(R)	73.8	70.8	95.9
6	ZIF-67/MWW(T)	55.5	52.9	95.3
7	ZIF-67	58.3	53.4	91.6
8	ZIF-67/MWW(P) ^b	52.2	44.7	85.6
9	Hmim	19.6	9.1	46.4
10	Co(NO ₃) ₂	78.4	20.6	26.3

Reaction conditions: HMF (0.1 g), ZIF-67/MWW(R) (20 mg) or catalysts of equimolar Co, acetone (5 mL), 150 °C, 4 h. ^aYield toward 4-[5-(hydroxymethyl)-2-furanyl]-3-buten-2-one (HMB). ^bPhysical mixture of Si-MWW and ZIF-67 powder.



support, Si-MWW, was used alone, it exhibited poor activity with a conversion of 15.7% (Table 3, entry 2). Moreover, exploratory experiments were conducted by using different catalysts with equimolar Co. Co/MWW showed low catalytic performance with a conversion of 30.7% and a yield of 8.4% (Table 3, entry 3), which indicated that Co ion grafted Si-MWW was not an effective catalyst for this reaction. In contrast, the ZIF-67/MWW(R) catalyst achieved a conversion of 73.8% and a yield of 70.8% (selectivity 95.9%) for the target product (Table 3, entry 5), while ZIF-67/MWW(U) showed a slightly lower conversion (64.9%) and (56.5%) yield (Table 3, entry 4). The slightly lower selectivity of HMB (87.0%, Table 3, entry 4) is mainly attributed to the uncovered Si-MWW zeolite, which contributes to a portion of the conversion. Additionally, under the same catalytic conditions, ZIF-67/MWW(T) exhibited inferior activity (conversion 55.5%, HMB yield 52.9%, Table 3, entry 6) compared to ZIF-67/MWW(R). This could be explained by the diffusion limitation caused by the larger size, particularly the tightly packed thick layer of ZIF particles (Fig. 6a),¹⁷ which hinders the mass transfer process and reduces the number of exposed active sites. This result is similar to that of conventional ZIF-67 (Table 3, entry 7), which may aggregate during the reaction. The Si-MWW support prevents the aggregation of ZIF-67 nanoparticles by surface anchoring, resulting in good dispersion and improved reaction performance. In contrast, the physical mixture of Si-MWW and ZIF-67 in the same weight ratio as that of ZIF-67/MWW(R) shows a low catalytic activity (conversion 52.2%, HMB yield 44.7%, Table 3, entry 8).

Further control experiments were conducted to evaluate the catalytic performance of the metal salt and organic ligand of ZIF-67. $\text{Co}(\text{NO}_3)_2$ exhibited a conversion of 78.4% and a yield of 20.6% for HMB under the same reaction conditions (Table 3, entry 10). The linker Hmim also showed poor catalytic performance with a conversion of 19.6% and a yield of 9.1% for HMB (Table 3, entry 9). This indicates that only the free metal ions or isolated linkers are not effective catalysts for producing HMB from HMF. We propose that the activity is contributed by the acid–base sites of ZIF-67 nanoparticles mounted on the Si-MWW surface, which are provided by the co-ordinately unsaturated metal and uncoordinated N, respectively, distributed at the structure edges and defects on ZIF-67 crystal surfaces.⁵ The NH_3 -TPD profile (Fig. S6, ESI†) confirms the acidity of the ZIF-67/MWW(R) catalyst, with a desorption peak observed at around 175 °C, indicating weak acidity. As depicted in Fig. S7, ESI†, the acid and base active species simultaneously play a role in the activation of acetone, leading to the formation of enol anions and enolate species, respectively.^{17,58} Furthermore, the Si-MWW zeolite framework structure stabilizes carbonyl species, facilitating a nucleophilic attack in the subsequent step of the reaction.⁵⁹

A time-dependent study was conducted under the same catalyst feeding conditions (Fig. 7). Within 4 h, the conversion of HMF and the yield of HMB gradually increased with prolonged reaction time, with ZIF-67/MWW(R) outperforming all other catalysts in terms of both conversion and yield.

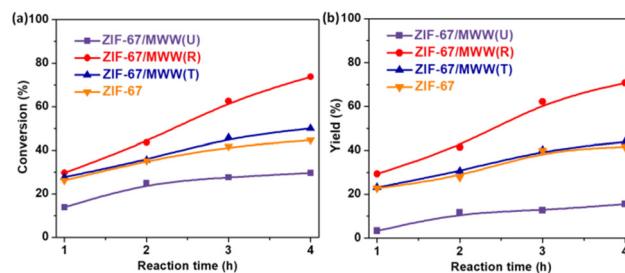


Fig. 7 (a) HMF conversion; (b) HMB yield versus reaction time over different catalysts, respectively. Reaction conditions: HMF (0.1 g) and catalyst (0.02 g) in acetone (5 mL), 150 °C.

The inferior activity of ZIF-67/MWW(U) is due to the insufficient number of ZIF-67 nanoparticles. ZIF-67/MWW(T) and ZIF-67 exhibited similar behavior, lying between ZIF-67/MWW(R) and ZIF-67/MWW(U) (Fig. 7a), which correlates with their aggregated forms.

The correlation between the ZIFs on the surface of MWW and the catalytic performance was explored by regulating the coverage level of ZIFs in the zeolite support. As displayed in Fig. S8, ESI†, the coverage level of ZIF-67 can be controlled in the following order: Si-MWW < ZIF-67/MWW(U) < ZIF-67/MWW(1/4) < ZIF-67/MWW(1/2) < ZIF-67/MWW(R) < ZIF-67/MWW(T). Furthermore, cobalt contents were analyzed by ICP elemental analysis, showing a proportional relationship with the coverage level of ZIF-67 (Table S1†). Intriguingly, the catalytic activity of ZIF-67/MWW exhibited a volcano-type relationship with respect to the content of Co (coverage level of ZIF-67) under the same catalyst feeding conditions (Fig. S9, ESI†). The catalytic activity of ZIF-67/MWW gradually increased with the content of Co (coverage level of ZIF-67) when ZIF-67/MWW(U), ZIF-67/MWW(1/4), ZIF-67/MWW(1/2) and ZIF-67/MWW(R) were used as catalysts. However, for ZIF-67/MWW(T), a marked reduction in catalytic activity was observed, which was mainly due to the mass transfer obstruction caused by the excessive coverage.

ZIF-67/MWW(R) catalyst was compared with those reported in previous literature, as shown in Table S2, ESI†. Previous literature demonstrated the use of MgZr and MgAl as catalysts, achieving conversions of 68.0% and 27.2%, with lower selectivities of target products (20.7% and 12.1%, Table S2, entries 1 and 2†), respectively.⁵⁷ Furthermore, MgO–ZrO₂ also showed inferior catalytic performance with a conversion of 68.5% and a selectivity of 48.6% for HMB (Table S2, entry 5†).⁶⁰ In addition, two zeolite-related catalysts displayed conversions of 68.3% and 51.4%, while the Hie-FAUZIF-8 catalyst achieved a selectivity of 97.8% for the target product, surpassing Nit-NaY (63.6%) (Table S2, entries 3 and 4†).^{17,60} In this work, the ZIF-67/MWW(R) catalyst showcased a better performance, a conversion of 73.8% with a selectivity of 95.9% was obtained in 4 h at 150 °C (Table S1, entry 6†). This comparative analysis highlights the remarkable advantages of the catalyst discussed in this work (Table S2†).



The recyclability test of the ZIF-67/MWW catalyst for the aldol condensation reaction is shown in Fig. 8. The data from this extended stability test indicate that ZIF-67/MWW retains its primary activity even after four runs. Furthermore, a product yield loss of approximately 3.1% was observed. The catalytic activity loss after four runs could be attributed to some possible factors, such as the interaction of oligomers with the catalyst and the potential loss of active sites, as reported in ref. 56, 57 and 60. The XRD patterns and SEM images of the used ZIF-67/MWW(R) indicate a well-preserved structure and morphology (Fig. S10 and 11, ESI†). These results suggest the good stability of the ZIF-67/MWW catalyst, which benefits from the stabilizing effect of the supported growth structure.

The substrate scope of the aldol condensation over ZIF-67/MWW(R) was investigated under the same reaction conditions. This experiment covered furfural, benzaldehyde, cinnamaldehyde, and some electron-donating or -withdrawing group substituted aromatic aldehydes, respectively. Furfural also underwent aldol condensation smoothly and afforded 34.6% yield (Table 4, entry 1), which was similar to what was previously reported in the literature.¹⁷ Moreover, when benzaldehyde, cinnamaldehyde, and aromatic aldehydes substituted with electron-donating groups (*e.g.*, -OMe) were employed (Table 4, entries 2–4), the target products were obtained in yields exceeding 86%. Similarly, for aromatic aldehydes substituted with electron-withdrawing groups (*e.g.*, -Cl and -CF₃), substantial yields of 80.5% and 87.5% were achieved for the corresponding target product (Table 4, entries 5 and 6). It is worth noting that the catalytic activity is gradually decreased when veratraldehyde, 3,4,5-trimethoxybenzaldehyde and amylcinnamaldehyde were used as substrates (Table 4, entries 7–9), which were attributed to the bulky substrates that enhance the mass transfer resistance and the steric effect. The additional findings demonstrated that the ZIF-67/MWW catalyst exhibits

Table 4 Aldol reactions of various aldehydes catalyzed by ZIF-67/MWW(R)

Entry	Substrate	Product	Con. (%)	Yie. (%)	Sel. (%)
1			44.3	34.6	78.1
2			91.5	86.2	94.2
3			95.3	87.2	91.5
4			100	92.5	92.5
5			100	80.5	80.5
6			100	87.5	87.5
7			60.5	54.5	90.1
8			43.8	43.7	99.9
9			19.9	12.5	62.8

Reaction conditions: aldehydes (0.8 mmol), catalyst (20 mg), acetone (5 mL), 150 °C, 4 h. Conversion and selectivity were determined by GC.

remarkable activity in the aldol reaction involving acetone and various aldehydes, highlighting its versatility (Table 4).

In addition, this approach could also be used to anchor other types of ZIF nanocrystals onto the Si-MWW surface, such as ZIF-8. XRD patterns (Fig. S12a, ESI†) and N₂ physisorption (Fig. S12b and Table S3, ESI†) of the ZIF-8/MWW(R) confirmed the presence of both ZIF-8 and Si-MWW. The SEM image (Fig. S13, ESI†) revealed that the ZIF-8 nanoparticles were densely attached to the surface of Si-MWW zeolite. Furthermore, due to the uniform anchoring of ZIF-8 on the surface of Si-MWW zeolite, the composite is endowed with the pore characteristics of both ZIF-8 and Si-MWW zeolite materials. The catalysis application study of ZIF-8/MWW(R) is currently in progress. Meanwhile, the ordered packed ZIF-8-on-MWW structure holds great promise in the field of gas separation as a hybrid membrane.⁶

4. Conclusions

In conclusion, the ZIF-67/MWW composite was successfully fabricated using a seeding-and-regrowth strategy. This involved grafting Co ions and anchoring ZIF-67 crystal seeds on the lamella Si-MWW zeolite surface, which played a vital role in achieving uniform growth of a ZIF-67 nanoparticle layer on Si-MWW. The Si-MWW zeolite, with its large in-plane surface and enriched Si-OH groups, not only acted as a host for the nanoparticles, but also enhanced the interaction between ZIF-67 and Si-MWW. This effectively hindered the aggregation

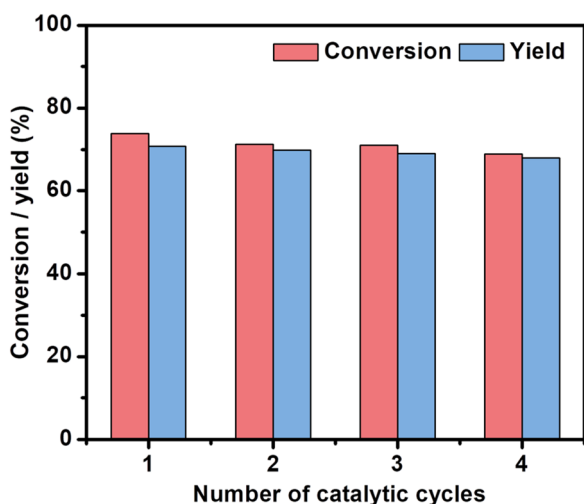


Fig. 8 Catalytic stability of the ZIF-67/MWW(R) catalyst for the aldol condensation. Reaction conditions: HMF (0.1 g), catalysts (20 mg), acetone (5 mL), 150 °C, 4 h.



of ZIF-67 nanoparticles during the growth process. The confined size and well-dispersed status of ZIF-67 on ZIF-67/MWW (R) resulted in excellent catalytic properties during the aldol condensation of various aldehydes with acetone. The acid-base sites from the exposed unsaturated Co and incompletely connected linkers of ZIF-67 served as the active centers. This approach opens up new avenues for integrating zeolites with MOFs to form composite nanocatalysts.

Author contributions

Author contributions: Tianlong Wang performed catalyst preparation, characterization, and the catalysis test and prepared the draft manuscript. Lin-an Liu participated in catalyst preparation and the catalysis test. Huifang Wu performed SEM imaging and N₂ adsorption. Jiaying Zhang performed the DRIFT test. Ziyi Feng performed TEM imaging. Xin Yan participated in zeolite synthesis. Xinyu Wang participated in catalyst preparation. Guoying Han participated in the catalysis test. Xiao Feng participated in the characterization, discussion of results and manuscript revision. Limin Ren designed the study, analyzed the data, and wrote the paper. Xinwen Guo supervised and revised the draft. Data and materials availability: all data are available in the manuscript or the ESI.†

Conflicts of interest

There are no conflicts to declare.

Acknowledgements

This work was supported by the National Natural Science Foundation of China (22002012). The Large Instrument and Equipment Open Foundation of the Dalian University of Technology and the Instrument Analysis Center of the Dalian University of Technology are acknowledged as well.

References

- H. Furukawa, K. E. Cordova, M. O'Keeffe and O. M. Yaghi, *Science*, 2013, **341**, 974–988.
- R. Banerjee, A. Phan, B. Wang, C. Knobler, H. Furukawa, M. O'Keeffe and O. M. Yaghi, *Science*, 2008, **319**, 939–943.
- B. Wang, A. P. Cote, H. Furukawa, M. O'Keeffe and O. M. Yaghi, *Nature*, 2008, **453**, 207–211.
- S. Furukawa, J. Reboul, S. Diring, K. Sumida and S. Kitagawa, *Chem. Soc. Rev.*, 2014, **43**, 5700–5734.
- Y. B. Huang, J. Liang, X. S. Wang and R. Cao, *Chem. Soc. Rev.*, 2017, **46**, 126–157.
- F. Rashidi, J. Leisen, S.-J. Kim, A. A. Rownaghi, C. W. Jones and S. Nair, *Angew. Chem., Int. Ed.*, 2019, **58**, 236–239.
- X. Ma, P. Kumar, N. Mittal, A. Khlyustova, P. Daoutidis, K. A. Mkhoyan and M. Tsapatsis, *Science*, 2018, **361**, 1008–1011.
- Q. Li, J. Guo, H. Zhu and F. Yan, *Small*, 2019, **15**, 1804874.
- W. Yao, J. Chen, Y. Wang, R. Fang, Z. Qin, X. Yang, L. Chen and Y. Li, *Angew. Chem., Int. Ed.*, 2021, **60**, 23729–23734.
- A. Phan, C. J. Doonan, F. J. Uribe-Romo, C. B. Knobler, M. O'Keeffe and O. M. Yaghi, *Acc. Chem. Res.*, 2010, **43**, 58–61.
- L. Zhou, H. Li, D. Wang, W. Jiang, Y. Wu, L. Shang, C. Guo, C. Liu and B. Ren, *Electroanalysis*, 2022, **34**, 1–12.
- M. B. Majewski, H. Noh, T. Islamoglu and O. K. Farha, *J. Mater. Chem. A*, 2018, **6**, 7338–7350.
- X. Cai, Z. Xie, D. Li, M. Kassymova, S. Q. Zang and H. L. Jiang, *Coord. Chem. Rev.*, 2020, **417**, 213366.
- A. Semrau, P. Stanley, A. Urstoeger, M. Schuster, M. Cokoja and R. Fischer, *ACS Catal.*, 2020, **10**, 3203–3211.
- A. Semrau, S. Pujari, P. Stanley, S. Wannapaiboon, B. Albada, H. Zuilhof and R. Fischer, *Chem. Mater.*, 2020, **32**, 9954–9963.
- K. Ma, K. B. Idrees, F. A. Son, R. Maldonado, M. C. Wasson, X. Zhang, X. Wang, E. Shehayeb, A. Merhi, B. R. Kaafarani, T. Islamoglu, J. H. Xin and O. K. Farha, *Chem. Mater.*, 2020, **32**, 7120–7140.
- D. Suttipat, W. Wannapakdee, T. Yutthalekha, S. Ittisanronnachai, T. Ungpittagul, K. Phomphrai, S. Bureekaew and C. Wattanakit, *ACS Appl. Mater. Interfaces*, 2018, **10**, 16358–16366.
- T. Imyen, E. Znoutine, D. Suttipat, P. Iadrat, P. Kidkhunthod, S. Bureekaew and C. Wattanakit, *ACS Appl. Mater. Interfaces*, 2020, **12**, 23812–23821.
- O. Singh, A. Agrawal, B. M. Abraham, R. Goyal, C. Pendem and B. Sarkar, *Mater. Today Chem.*, 2022, **24**, 100796.
- J. Li, A. Corma and J. Yu, *Chem. Soc. Rev.*, 2015, **44**, 7112–7127.
- X. Meng and F. S. Xiao, *Chem. Rev.*, 2014, **114**, 1521–1543.
- C. Martinez and A. Corma, *Coord. Chem. Rev.*, 2011, **255**, 1558–1580.
- N. Yuan, X. Zhang and L. Wang, *Coord. Chem. Rev.*, 2020, **421**, 213442.
- H. Guo, X. Lu, J. He, H. Zhang, H. Zhang, Y. Dong, D. Zhou and Q. Xia, *Mater. Chem. Phys.*, 2023, **294**, 127001.
- L. H. Chen, M. H. Sun, Z. Wang, W. Yang, Z. Xie and B. L. Su, *Chem. Rev.*, 2020, **120**, 11194–11294.
- M. Hartmann, M. Thommes and W. Schwieger, *Adv. Mater. Interfaces*, 2021, **8**, 2001841.
- A. Corma, C. Corell and J. Pérez-Pariente, *Zeolites*, 1995, **15**, 2–8.
- A. Corma, V. Fornés, S. B. Pergher, T. L. M. Maesen and J. G. Buglass, *Nature*, 1998, **396**, 353–356.
- L. Liu, U. Díaz, R. Arenal, G. Agostini, P. Concepción and A. Corma, *Nat. Mater.*, 2017, **16**, 132–138.
- H. Y. Luo, V. K. Michaelis, S. Hodges, R. G. Griffin and Y. Román-Leshkov, *Chem. Sci.*, 2015, **6**, 6320–6324.
- X. Ouyang, S. J. Hwang, R. C. Runnebaum, D. Xie, Y. J. Wanglee, T. Rea, S. I. Zones and A. Katz, *J. Am. Chem. Soc.*, 2014, **136**, 1449–1461.



- 32 Y. Zhou, Y. Mu, M. F. Hsieh, B. Kabius, C. Pacheco, C. Bator, R. M. Rioux and J. D. Rimer, *J. Am. Chem. Soc.*, 2020, **142**, 8211–8222.
- 33 W. Zhang, Y. Zhou, M. Shamzhy, S. Molitorisová, M. Opanasenko and A. Giroir-Fendler, *ACS Appl. Mater. Interfaces*, 2021, **13**, 15143–15158.
- 34 P. He, Q. Yi, H. Geng, Y. Shao, M. Liu, Z. Wu, W. Luo, Y. Liu and V. Valtchev, *ACS Catal.*, 2022, **12**, 14717–14726.
- 35 T. Wang, H. Ma, J. Gao, X. Wang, Y. Sun, Y. Luo, S. Zhang and J. Xu, *Chem. – Asian J.*, 2017, **12**, 2790–2793.
- 36 T. Wang, W. Huang, H. Han, J. Zhang, H. Wu, X. Yan, Y. Jiang, L. Fang, B. Zhang, X. Guo and L. Ren, *Inorg. Chem. Front.*, 2022, **9**, 3505–3513.
- 37 S. Maheshwari, E. Jordan, S. Kumar, F. S. Bates, R. L. Penn, D. F. Shantz and M. Tsapatsis, *J. Am. Chem. Soc.*, 2008, **130**, 1507–1516.
- 38 J. Qin, S. Wang and X. Wang, *Appl. Catal., B*, 2017, **209**, 476–482.
- 39 H. Li, H. Ma, X. Wang, J. Gao, C. Chen, S. Shi, M. Qu, N. Feng and J. Xu, *J. Energy Chem.*, 2014, **23**, 742–746.
- 40 X. Wei, W. Pan, X. Li, M. Pan, C. Huo, R. Yang and Z. Chao, *Chem. Mater.*, 2019, **32**, 333–340.
- 41 R. A. Borse, M. B. Kale, V. S. Hakke, N. Pandi, S. H. Sonawane and Y. Wang, *Adv. Mater. Interfaces*, 2022, **10**, 1–10.
- 42 K. Zhao, H. Li, S. Tian, W. Yang, X. Wang, A. Pang, C. Xie and D. Zeng, *Inorg. Chem. Front.*, 2019, **6**, 715–722.
- 43 W. Li, Y.-Y. Liu, Y. Bai, J. Wang and H. Pang, *J. Hazard. Mater.*, 2020, **395**, 122692.
- 44 N. A. Grosso-Giordano, A. S. Hoffman, A. Boubnov, D. W. Small, S. R. Bare, S. I. Zones and A. Katz, *J. Am. Chem. Soc.*, 2019, **141**, 7090–7106.
- 45 Y. Pan, A. Bhowmick, W. Wu, Y. Zhang, Y. Diao, A. Zheng, C. Zhang, R. Xie, Z. Liu, J. Meng and D. Liu, *ACS Catal.*, 2021, **11**, 9970–9985.
- 46 H. K. Min, S. Kweon, S. Oh, H. An, Y. Cho, H. Min, D. Jo, J. F. Kim, C. H. Shin, S. B. Kang and M. B. Park, *Green Chem.*, 2021, **23**, 9489–9501.
- 47 G. Liu, J. Jiang, B. Yang, X. Fang, H. Xu, H. Peng, L. Xu, Y. Liu and P. Wu, *Microporous Mesoporous Mater.*, 2012, **165**, 210–218.
- 48 M. M. J. Treacy and J. M. Newsam, *Nature*, 1988, **332**, 249–251.
- 49 J. Zhang, A. Zhou, K. Gawande, G. Li, S. Shang, C. Dai, W. Fan, Y. Han, C. Song, L. Ren, A. Zhang and X. Guo, *ACS Catal.*, 2023, **13**, 3794–3805.
- 50 X. Zhang, D. Liu, D. Xu, S. Asahina, K. A. Cychosz, K. V. Agrawal, Y. A. Wahedi, A. Bhan, S. A. Hashimi, O. Terasaki, M. Thommes and M. Tsapatsis, *Science*, 2012, **336**, 1684–1687.
- 51 Z. Zhu, H. Xu, J. Jiang, X. Liu, J. Ding and P. Wu, *Appl. Catal., A*, 2016, **519**, 155–164.
- 52 B. Tang, S. Li, W.-C. Song, E.-C. Yang, X.-J. Zhao, N. Guan and L. Li, *ACS Sustainable Chem. Eng.*, 2019, **7**, 16329–16343.
- 53 L. Liu, J. Lu, Y. Yang, W. Ruettinger, X. Gao, M. Wang, H. Lou, Z. Wang, Y. Liu, X. Tao, L. Li, Y. Wang, H. Li, H. Zhou, C. Wang, Q. Luo, H. Wu, K. Zhang, J. Ma, X. Cao, L. Wang and F.-S. Xiao, *Science*, 2024, **383**, 94–101.
- 54 S. Zhang, H. Ma, Y. Sun, Y. Luo, X. Liu, M. Zhang, J. Gao and X. Jie, *Green Chem.*, 2019, **21**, 1702–1709.
- 55 E. Hayashi, Y. Yamaguchi, K. Kamata, N. Tsunoda, Y. Kumagai, F. Oba and M. Hara, *J. Am. Chem. Soc.*, 2019, **141**, 890–900.
- 56 R. S. Malkar, H. Daly, C. Hardacre and G. D. Yadav, *ACS Sustainable Chem. Eng.*, 2019, **7**, 16215–16224.
- 57 J. Cueto, L. Faba, E. Díaz and S. Ordóñez, *Appl. Catal., B*, 2017, **201**, 221–231.
- 58 T. Yutthalekha, D. Suttipat, S. Salakhum, A. Thivasasith, S. Nokbin, J. Limtrakul and C. Wattanakit, *Chem. Commun.*, 2017, **53**, 12185–12188.
- 59 S. Yadnum, S. Choomwattana, P. Khongpracha, J. Sirijaraensre and J. Limtrakul, *ChemPhysChem*, 2013, **14**, 923–928.
- 60 W. Shen, G. A. Tompsett, K. D. Hammond, R. Xing, F. Dogan, C. P. Grey, W. C. Conner, S. M. Auerbach and G. W. Huber, *Appl. Catal., A*, 2011, **392**, 57–68.

